

Machine learning approach for modeling daily pluvial flood dynamics in agricultural landscapes

Emine Fidan ^{a,b}, Josh Gray ^{c,d}, Barbara Doll ^{a,e}, Natalie G. Nelson ^{a,c,*}

^a Biological and Agricultural Engineering, North Carolina State University, Raleigh, NC, USA

^b Biosystems Engineering and Soil Science, University of Tennessee, Knoxville, TN, USA

^c Center for Geospatial Analytics, North Carolina State University, Raleigh, NC, USA

^d Forestry and Environmental Resources, North Carolina State University, Raleigh, NC, USA

^e North Carolina Sea Grant, Raleigh, NC, USA



ARTICLE INFO

Handling Editor: Daniel P Ames

ABSTRACT

Despite rural, agricultural landscapes being exposed to pluvial flooding, prior predictive flood modeling research has largely focused on urban areas. To improve and extend pluvial flood modeling approaches for use in agricultural regions, we built a machine learning model framework that uses remotely sensed imagery from Planet Labs, gridded rainfall data, and open-access geospatial landscape characteristics to produce a pluvial flood timeline. A Random Forest model was trained and daily flood timeline was generated for Hurricane Matthew (2016) at a 10-m resolution. The results show the model predicts pluvial flooding well, with overall accuracy of 0.97 and F1 score of 0.69. Further evaluation of model outputs highlighted that corn and soybean crops were most impacted by the pluvial flooding. The model may be used to identify agricultural areas susceptible to pluvial flooding, crops that may be potentially impacted, and characteristics of areas that experience pluvial flooding.

1. Introduction

Floods are the most common and costliest natural hazard in the United States (USA) and world (NOAA NSSL, n.d.; WHO, n.d.). In the USA, many people are impacted by flood disasters, with financial losses from flood exposure amounting to over 2.5 billion dollars in 2021 alone (NOAA NCEI, 2021). Flooding can occur in different forms: fluvial, coastal, and pluvial. Fluvial flooding is the result of water overflowing the boundaries of a channel, coastal flooding is induced by tides and storm events, and pluvial flooding occurs when heavy rainfall introduces more water than the drainage capacity of the landscape. In particular, pluvial flooding (sometimes referred to as surface water flooding) is often used to describe inundation that occurs outside of floodplains surrounding river networks. Historically, research on flooding has focused on fluvial and coastal mechanisms with pluvial flooding being understudied in comparison (Muthusamy et al., 2019). As a result, more effort has been invested towards analyzing and mitigating fluvial and coastal flooding impacts (Muthusamy et al., 2019). Moreover, of studies that have aimed to advance understanding of pluvial flood dynamics, most have used urban areas as study systems (e.g., Abebe et al., 2018;

Guerreiro et al., 2017; Li et al., 2021; Palla et al., 2018; van Dijk et al., 2013).

Although characterizing pluvial flooding in urban settings is important for protecting public health and safety, rural areas also face comparable risks. In particular, crops are sensitive to waterlogging and anaerobic soil conditions; thus, the agricultural sector is prone to detrimental pluvial flood impacts ranging from economic loss to food insecurity at local and global scales (Tanir et al., 2021). With pluvial flooding leading to damages to crops and livestock, having the ability to predict pluvial flood extent in agricultural landscapes is necessary for identifying vulnerable areas and preparing for flood-driven impacts. Flood models are used by natural resource managers, insurance companies, emergency responders, and policymakers to better understand historical flood dynamics, as well as identify areas of future flood risk. Model outputs, in return, can inform the development of management actions and policies to minimize the impact of flood disasters and manage the agricultural resources accordingly, as recent studies show that more areas are vulnerable to flooding than current flood maps show (First Street Foundation, 2020; Tellman et al., 2021). In particular, pluvial flood predictions could be used for crop insurance purposes, so as

* Corresponding author. Campus Box 7625, Raleigh, NC, 27695, USA.

E-mail address: nnelson4@ncsu.edu (N.G. Nelson).

to identify areas of crop damage, manage susceptible areas with high flood hazard risk, and estimate fiscal damages.

Despite the benefits of modeling pluvial flood dynamics, reliably quantifying pluvial flood extent in agricultural landscapes is challenging due to agricultural lands often spanning flat terrains outside of delineated floodplains, and including drainage networks that are poorly mapped relative to natural river channels and tributaries. In addition, modeling pluvial flooding in flat terrains outside of delineated floodplains is often difficult due to the complex and chaotic nature of flood hydraulics (Bernet et al., 2018; Bulti and Abebe, 2020).

Approaches for modeling flooded areas include using process-based modeling and data-driven modeling methods (Teng et al., 2017). Physically based models like HEC-RAS and MIKE FLOOD apply the laws of fluid motion to simulate hydrodynamic processes, thus making this class of flood models an ideal choice for producing dynamic flood estimates. Applications of process-based flood models have been reviewed by Kauffeldt et al. (2016), Teng et al. (2017), Jain et al. (2018), Bulti and Abebe (2020), and Qi et al. (2021). Despite their strengths, many studies have also highlighted the challenges with process-based modeling techniques – generally speaking, physically based models require well-defined boundary conditions, an understanding of complex drainage systems, abundance of validation data, expert domain knowledge, and use of high computational power (Choubin et al., 2019; Zakaria et al., 2021).

Data-based or empirical methods in flood modeling are able to provide flood extent estimates without explicit physical process representation and serve as valuable alternatives to physically-based flood models. Traditionally, data-driven flood models have consisted of time-series statistical models, such as linear regression, autoregressive moving average, and auto-regressive integrated moving average (Zakaria et al., 2021). However, recent research has moved away from time-series statistical methods due to their inability to capture non-linear hydrological dynamics, and underlying assumptions regarding normality and stationarity (Zakaria et al., 2021). Machine learning-based data-driven models have gained momentum, particularly as they are well-suited to capture non-linear flood dynamics and often outperform traditional flood modeling methods (Mosavi et al., 2018). Recent studies have demonstrated how support vector machines (e.g. Tehrany et al., 2019), multilayer perceptrons (e.g. Zakaria et al., 2021), decision trees (e.g. Tehrany et al., 2019; Khosravi et al., 2018), adaptive neuro-fuzzy inference systems (e.g. Zakaria et al., 2021; Tabbusum and Dar, 2021), wavelet neural networks (e.g. Yeditha et al., 2020), ensemble prediction systems (e.g. Towfiqul Islam et al., 2021), and other machine learning approaches (e.g. Costache et al., 2020; Kan et al., 2020; Kabir et al., 2021) are effective at predicting flooding using minimal inputs and low computational cost as compared to process-based modeling methods, showing promise for their use as predictive tools of flooding. Although machine learning models require substantial training data, we can obtain this data readily through remote sensing, which is accessible and does not require *in situ* data collection.

Overall, we sought to improve and extend previous urban pluvial flood modeling approaches for use in rural agricultural regions, specifically by building a machine learning flood model that uses satellite remote sensing, rainfall, and readily-available geospatial landscape characteristics to produce flood extent maps. Our objectives were to 1) develop a pluvial flood training and validation set using high spatio-temporal resolution optical satellite imagery from Planet Labs, 2) test the suitability of Random Forest for pluvial flood extent modeling in low-lying and flat agricultural terrain using rainfall and physiographic characteristics as predictors, 3) analyze predictor importance to understand key variables in the model, and 4) generate pluvial flood time series using the model. We specifically focus on a community in the flat, agriculturally-dominated landscape of the North Carolina (NC) Coastal Plain, USA, as a representative study system, and analyzed flooding across a major flood event that occurred as a result of Hurricane Matthew (2016). The pluvial flooding modeled in this work is

considered to be the flood extent outside the boundaries of the channel and floodplain. The methodological framework developed here is transferable to other agricultural areas, particularly those in low terrain landscapes, and demonstrates how satellite remote sensing observations and machine learning can be used to produce pluvial flood extent time series in rural catchments.

2. Materials and methods

2.1. Study area

We focused on the city of Kinston, NC, USA (671 km^2) which is located in the low-lying Coastal Plain of eastern NC (Fig. 1). Kinston was selected as the study area due to its vulnerability to extreme flooding, the spatial extent of available remotely sensed data, and extensive agricultural land (row crops and animal production). The predominant land cover in the study area consists of cultivated crops, followed by woody wetlands, evergreen forests, developed open spaces, shrub/scrub lands, and low intensity developed lands; these land cover classes are defined by the 2016 US National Land Cover Database (NLCD; Dewitz, 2019). As for the hurricane events, we considered three major hurricanes that impacted the NC Coastal Plain: Floyd (1999), Matthew (2016), and Florence (2018). High spatio-temporal resolution imagery was not available for Hurricane Floyd. Hurricane Matthew had three dates of available imagery at high resolution. Hurricane Florence had one image five days after landfall. Although one image was available for Hurricane Florence, we did not include it in this analysis as the single image captured days after landfall was considered insufficient for pluvial flood model training and testing purposes. Ultimately, the study region was delineated using the footprints of available imagery during the Hurricane Matthew aftermath.

Hurricane Matthew created massive flooding in Kinston when it impacted the Carolinas on October 8, 2016. Matthew initially impacted the Greater Antilles as a category 5 storm before making landfall along the central coast of South Carolina and bringing heavy rainfall (Stewart, 2017). Total rainfall from September 28 to October 9 in Kinston was 419 mm, or 16.50 inches, which is currently estimated to correspond to an approximately 500-year event (Stewart, 2017).

2.2. Delineating flooded areas from Planet Labs imagery

In order to create a dynamic flood model, remotely sensed imagery was processed into flood maps that served to train the model and test it. Planet Labs imagery was selected for this study as it offers daily optical imagery around the world at high resolutions ($<5\text{-m}$). Optical surface reflectance data from Planet Labs, specifically PlanetScope and RapidEye imagery, were selected instead of radar imagery due to the high spatio-temporal resolution, accessibility, and processing ease of these products. PlanetScope and RapidEye products offer imagery at 3–5 m resolution almost daily, which was resampled to 10-m to match the resolution of the predictor variable rasters. Imagery was downloaded for the flooding following Hurricane Matthew (October 8–15, 2016). Although Planet Labs imagery is available nearly every day, due to cloud cover obstruction from hurricane events, not all imagery could be used in this study. Images with greater than 30% cloud coverage were excluded. After excluding data with poor quality due to cloud cover, three remotely sensed images were available for Hurricane Matthew (Fig. 2). The available imagery included a PlanetScope image on Oct. 9, RapidEye image on Oct. 10, and PlanetScope image on Oct. 15 (image scenes available in supplemental material; Table S1). Although imagery was not available on the day of peak rainfall (i.e., hurricane landfall), we assume that there were delays with ponding since the soils needed to reach saturation capacity and the runoff from cumulative rainfall may have created a temporal delay in flooding. Therefore, peak rainfall may not coincide at the same time as the peak pluvial flooding.

Optical imagery presents issues with canopy penetration; therefore,

could
compute
experience
help?

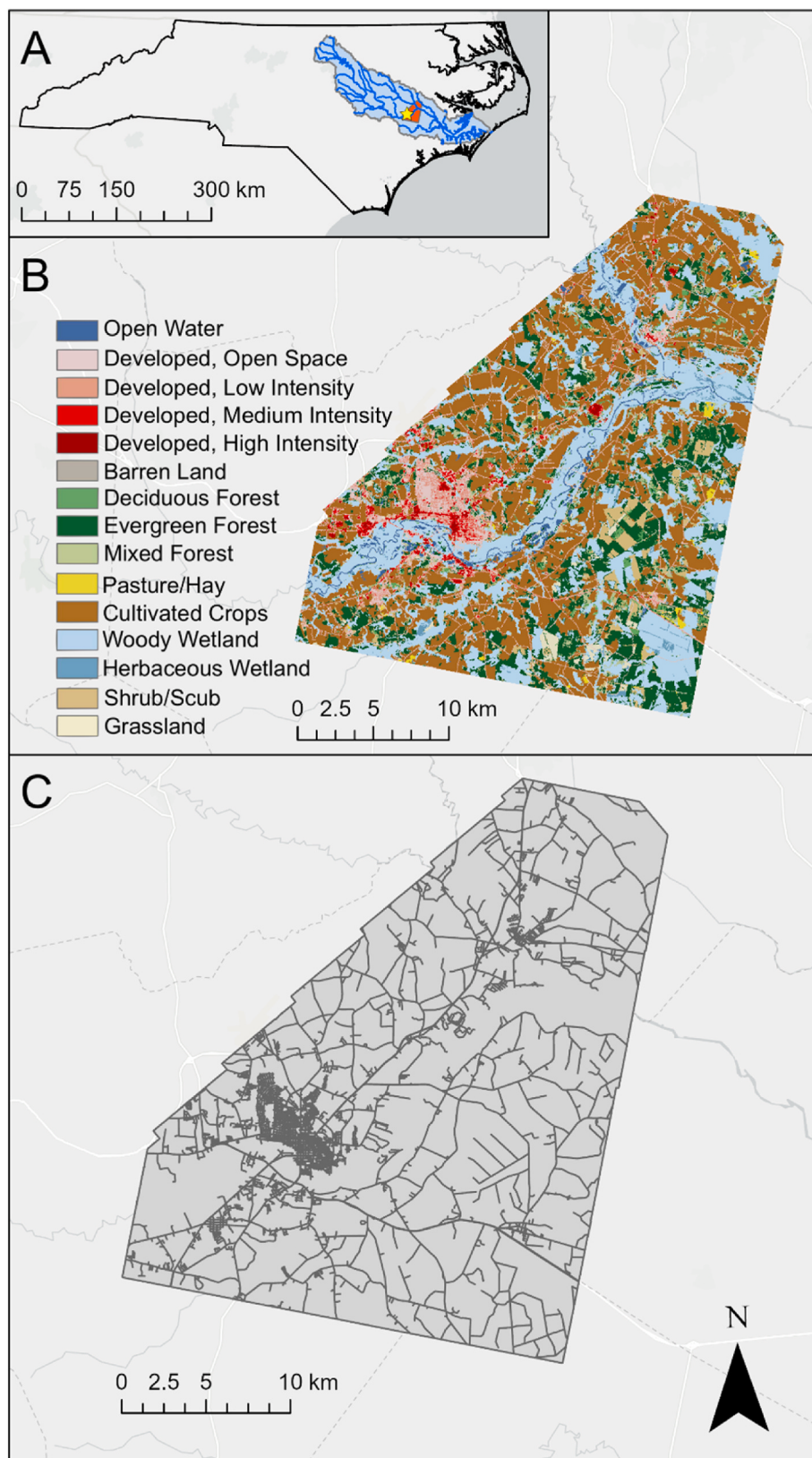


Fig. 1. Map of the study area showing (A) the extent of North Carolina with the red region representing the location of the study area, the yellow star indicating the town of Kinston, the light blue area showing the Neuse watershed, and the blue lines showing the Neuse River, (B) the different land cover classifications (Dewitz, 2019) in the study area, (C) the road network in the study area (U.S. Census Bureau, 2015).

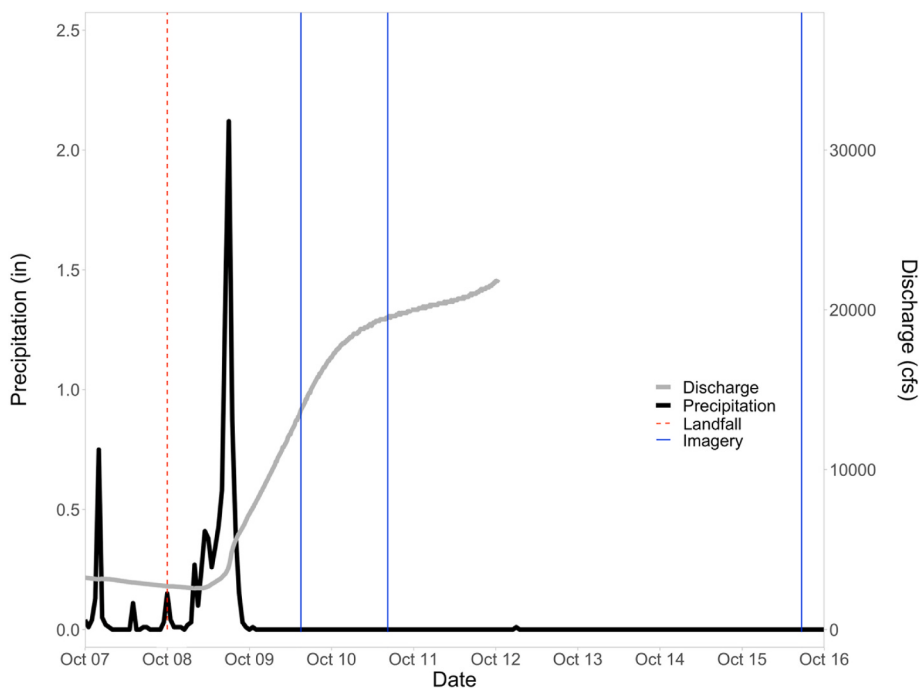


Fig. 2. The progression of rainfall and discharge with the corresponding Planet Labs imagery for Hurricane Matthew in the Kinston, NC area. The red dotted line represents the date of landfall. The blue vertical lines represent days in which imagery was available. All dates and times are in local time (EDT). Note that there is missing discharge data after Oct. 12.

inundation within forested and woody areas could not be analyzed with this product and were consequently masked from this analysis. Furthermore, due to the agricultural focus of this study, only potential agricultural landscapes were analyzed, while all other lands were masked. In this case, the land classifications were determined using the NLCD 2016. The NLCD is a categorical product produced at a 30-m resolution by a group of federal agencies known as the Multi-Resolution Land Characteristics (MRLC) consortium. This product was resampled from 30-m to 10-m using the nearest-neighbor method. We assumed that the land cover and land use did not vary within the 30-m by 30-m pixels given the minimal variation in land cover and land use across the rural and predominantly agricultural study area. The land cover pixels are classified as being Open Water; Developed, Open Space; Developed, Low Intensity; Developed, Medium Intensity; Developed, High Intensity; Barren Land; Deciduous Forest; Evergreen Forest; Mixed Forest; Shrubs; Grassland; Pasture Land; Cultivated Crop Land; Woody Wetland; or Herbaceous Wetland. Therefore, all land classifications except grasslands, cultivated croplands, and pasture lands were masked.

Additionally, we assume that pluvial flooding consists of flooding occurring in landscapes outside the boundaries of the river channels and floodplain. Accordingly, the floodplain areas as defined by the gridded FEMA National Flood Hazard Layer dataset (FEMA, 2019) were masked from the training data. After the masking of floodplains and non-agricultural land cover classes, 34% of the original area was kept for model development. Lastly, a scene classification (SCL) file was available for Planet Lab imagery; however, due to this product being inadequate for automated cloud detection, the cloud and cloud shadow pixels had to be masked manually.

From the available Planet Labs images, the Normalized Difference Water Index (NDWI) was applied to delineate standing water (Equation (1); McFeeters 1996). The NDWI ranges from values of -1 to 1, in which values closer to -1 indicate dry/vegetative pixels and values closer to 1 indicate water pixels.

$$NDWI = \frac{green - nir}{green + nir} \quad (1)$$

In Equation (1), green is the green band (typically ranging from 500 to 590 nm) and nir is the near infrared band (ranging from 760 to 860 nm). The equation was applied to each pixel in each image.

Although the NDWI highlights areas of standing water, a threshold value must be set in order to classify areas as either flooded or not flooded. To obtain a threshold value, high-resolution (15-cm) aerial imagery sparsely collected by the US National Oceanographic and Atmospheric Administration (NOAA) Emergency Response program was separately analyzed to determine which areas were flooded/non-flooded, and then compared to the satellite imagery NDWI values. Unfortunately, Hurricane Matthew did not have Planet Labs imagery with the same acquisition time as the NOAA Rapid Response aerial imagery, but Hurricane Florence had an overlap in the data. NOAA Emergency Response aerial imagery for Hurricane Florence was collected in the Kinston area on September 19, 2018, a date for which Planet Labs imagery was also available for NDWI value comparisons. A total of 2500 10-m by 10-m sample tiles were randomly generated from the NOAA aerial imagery and manually labeled as either flooded or not flooded depending on whether the floodwater fraction was $\geq 50\%$ flooded or $< 50\%$ not flooded, respectively. To quantify floodwater fraction, each 10-m by 10-m sample tile was split into 10x10 grids so the flooded pixels could be counted (Fig. S1). 2500 samples were chosen according to Equation (2), which estimates the standard error of the overall accuracy, i.e., the classification accuracy (CA), given a number of samples (n), assuming that the samples are a small proportion of the entire dataset such that this proportion is effectively zero. To determine the number of samples required, we solved for n in Equation (2), using a conservative CA of 0.5 and a standard error (SE) of 0.01. NOAA aerial imagery tiles within masked landscapes were later removed and not considered during subsequent analysis.

$$SE = \sqrt{CA * (1 - CA)/n} \quad (2)$$

Using the labeled NOAA aerial imagery data and NDWI values calculated from Planet Labs imagery, a receiver operator characteristic (ROC) analysis was performed to determine which NDWI value would be the best threshold when partitioning flood/non-flood conditions. The

ROC analysis balanced sensitivity and specificity to find the optimum NDWI threshold value for separating pixels into flood and non-flood classes. Specifically, the ROC analysis works by calculating the true positive rate and false positive rate of the data at different NDWI thresholds and summarizing which threshold had the highest true positive and lowest false positive rate. Using this approach, binary flood extent maps were created using NDWI from the Planet imagery. Fig. 3 represents the complete workflow used to generate the training data.

2.3. Processing predictor variable data

In building the machine learning model, predictor variables must be supplied to generate relationships between the response and the predictors. However, prior to supplying the predictor variables and building the model, the variables were screened for multicollinearity by analyzing the variance inflation factor (VIF; Marquardt, 1970). Screening predictor variables for multicollinearity is important since

high multicollinearity between two variables implies that those features are redundant. The predictor variables screened within the model were a combination of geophysical and hydrologic geospatial rasters (Table 1). The variables screened for the model were flood frequency, drainage class, elevation, height above nearest drainage, slope, topographic wetness, distance to nearest stream, distance to nearest road, and population density. In addition, a dynamic variable, precipitation, was included to capture the daily dynamics of flooding since all other variables are temporally static.

The flood frequency dataset, derived from the gSSURGO soils data product, was used to indicate documented susceptibility to flooding. gSSURGO flood frequency classes ranged from none (i.e., no history of flooding), very rare, rare, occasional, frequent, and very frequent; and these classifications are determined by the annual probability of an area to flood. Similarly, drainage class was also derived from the gSSURGO product and it was used within the model since areas with poor drainage are prone to standing water and inundation. The drainage classes ranged

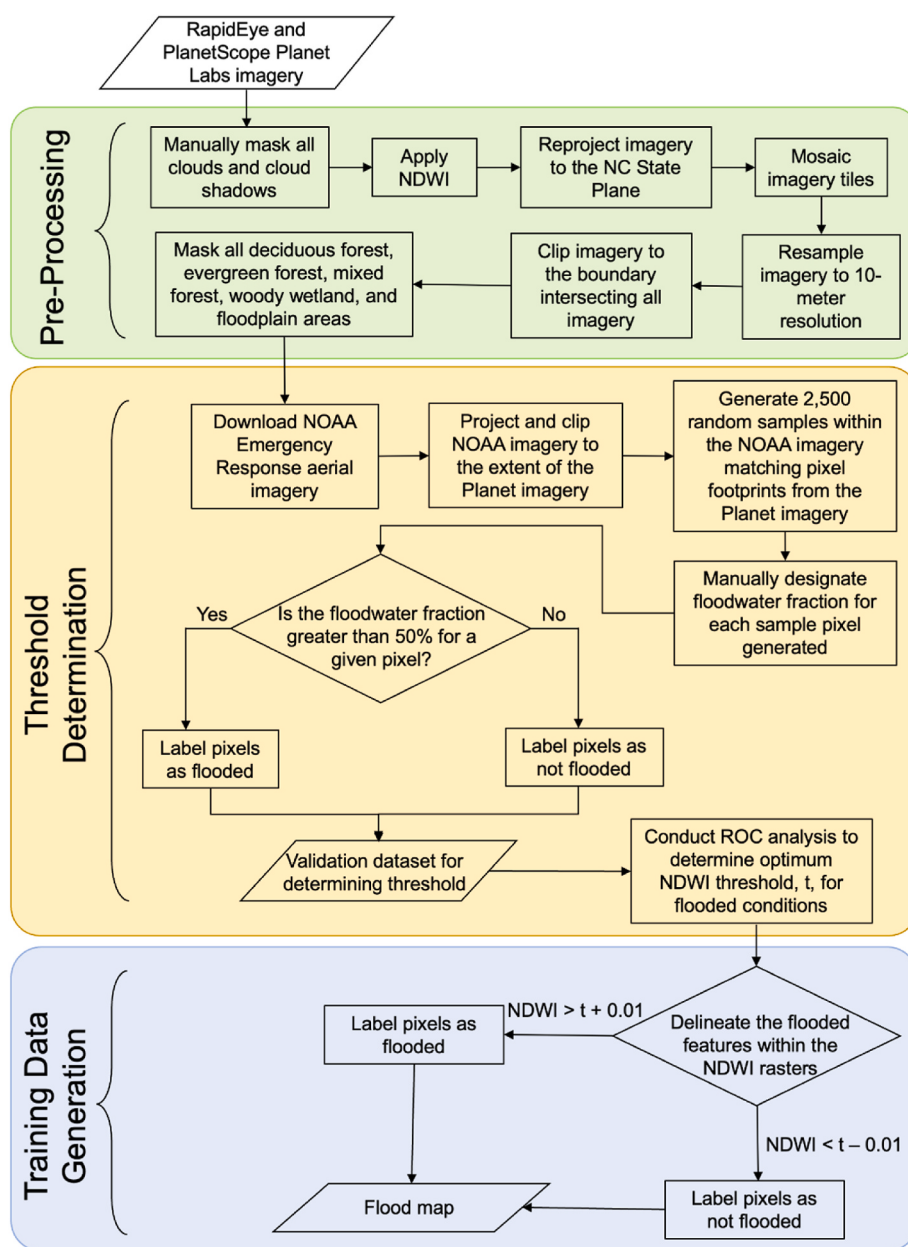


Fig. 3. Workflow used to generate pluvial flood maps from remotely sensed imagery. Rectangles correspond to processing steps, parallelograms indicate data products, and diamonds indicate decision steps.

Table 1

Predictor variables screened during model development. Native resolution is not included for derivative products or distance variables produced from vector data. Additionally, references are not included for derivative products created for this study.

Variable	Product Name/Source	Property	Data type	Native resolution	Reference
Flood Frequency	Gridded Soil Survey Geographic (gSSURGO) - Natural Resources Conservation Service	static	categorical	10-m	Soil Survey Staff, 2019
Drainage Class	Gridded Soil Survey Geographic (gSSURGO) - Natural Resources Conservation Service	static	categorical	10-m	Soil Survey Staff, 2019
Elevation	National Elevation Dataset - U.S. Geological Survey	static	continuous	10-m	U.S. Geological Survey, 2019a
Height Above Nearest Drainage	Calculated using Elevation	static	continuous		
Slope	Calculated using Elevation	static	continuous		
Topographic Wetness Index	Calculated using Elevation	static	continuous		
Distance to Nearest Stream	National Hydrography Dataset - U.S. Geological Survey	static	continuous		U.S. Geological Survey, 2019b
Distance to Nearest Road	U.S. Census Bureau	static	continuous		U.S. Census Bureau, 2015
Population	LandScan 2019 - Oak Ridge National Lab	static	continuous	1-km	Rose et al. (2020)
Precipitation	DayMet v3 - Oak Ridge National Lab	dynamic	continuous	1-km	Thornton et al. (2020)

from excessively drained, somewhat excessively drained, moderately well drained, well drained, somewhat poorly drained, poorly drained, and very poorly drained.

Elevation and derivative products were screened as predictors within the model to capture the physical processes of flooding, as elevation, height above nearest drainage, slope, and topographic wetness are all important indicators of flow movement and accumulation. Elevation was used as a predictor since lower elevations experience more flooding ([Botzen et al., 2012](#)), but it was also used to derive other terrain variables: height above nearest drainage, slope, and the topographic wetness index. Slope is an important terrain variable used as a proxy for runoff potential and infiltration time ([Tehrany et al., 2015](#)); it was calculated using the Slope tool within ArcGIS Pro. The height above nearest drainage and topographic wetness index variables were calculated and screened as predictor variables. Height above nearest drainage represents the difference in elevation between an area and its nearest drainage source ([Rennó et al., 2008](#)). Topographic wetness index highlights an area's potential to retain water and considers terrain influences on hydrological processes ([Tehrany et al., 2015](#)). To create these variables, the elevation dataset was first processed to fill sinks, then flow direction and flow accumulation were calculated using ArcGIS Pro version 2.3.0 to finally derive the height above nearest drainage and topographic wetness index.

In addition, distance to nearest stream and distance to nearest road were variables considered as predictors within the model. The distance to nearest stream variable was considered since high flows from riverine discharge have the capability to store water in a manner that affects the drainage capacity of nearby soils outside the delineated floodplain. Additionally, distances to nearest road data were used since roads typically drain water to the shoulders to avoid pooling on the surface of the pavement. Within North Carolina, roadway design standards indicate shoulder slopes on the outer edges of roads must allow for drainage ([NCDOT, 2002; NCDOT, 2018](#)). Thus, roads serve as important first order drainage systems within areas such as Kinston. Road and stream network data were obtained as vector files. The distance to nearest road and distance to nearest stream were calculated using the ArcGIS Pro Euclidean Distance tool, and then rasterized using the Vector to Raster tool. Note that we considered using flow path distance to streams; however, due to the flat topography and presence of unmapped artificial drainage systems, we were concerned that our flow path calculations would not be accurate and chose to use a simpler Euclidean distance approach.

The population variable was a 1-km resolution raster produced at a global extent. This dataset was bilinearly resampled to a 10-m resolution to match the resolution of the other datasets and renamed as population density rather than population count. Population density was used as a

possible predictor since areas with more people are highly correlated with an increase in flood cases ([Jongman et al., 2012](#)).

Rainfall was used as a dynamic predictor variable to capture day-to-day changes in flooding. Precipitation data was derived from the Oak Ridge National Laboratory DayMet product ([Thornton et al., 2020](#)). This gridded product measures daily precipitation at 1-km resolution, thus the raster was resampled down to 10-m resolution using the bilinear resampling method. In this case, we assume homogeneity within the 1-km² pixels. DayMet v3 reports rainfall between 0 and 200 mm, and areas that received greater than 200 mm (7.9 inches) of rainfall were assigned the maximum value of 200 mm. DayMet data are available at a daily timestep, and were used to generate seven predictor variables that were screened in the model: daily, 2-day antecedent, 3-day antecedent, 4-day antecedent, 5-day antecedent, 6-day antecedent, and 7-day antecedent rainfall. All precipitation variables were totals, e.g. the 2-day antecedent variable consisted of the total, cumulative rainfall over a 2-day period. The antecedent rainfall derivatives were calculated using R software version 4.0.2 ([R Core Team, 2020](#)). These products were used to capture the compounding influence of precipitation and rainfall runoff on pluvial flooding.

Lastly, land cover was considered as a predictor within the model since the surface of the land has a strong influence on the capability of rain to infiltrate or generate runoff. Due to the focus on agricultural landscapes within this study, all land classifications except grasslands, cultivated croplands, and pasture lands were masked. Thus, due to the similar characteristics of these potential agricultural lands, the land cover dataset was not used as a predictor within the model.

2.4. Model training and testing

2.4.1. Random Forest

A Random Forest model was chosen due to its versatility, relatively low computational power demands, and ability to handle high dimensional data (e.g. [Chen et al., 2020; Hou et al., 2021; Kabir et al., 2021; Motta et al., 2021](#)). The Random Forest algorithm is a machine learning model that randomly subsets a sample of the data and predictors, trains a decision tree to the sampled values, and repeats the sampling and training process n times ([Breiman, 2001](#)). The final model consists of many decision trees that are individually unskilled, but collectively effective at prediction ([Dietterich, 2000](#)). To train the Random Forest algorithm, the ranger package in R version 4.0.2 was used due to its computational efficiency as compared to other Random Forest packages ([Wright and Ziegler, 2017](#)). The Random Forest model was trained as a binary classifier of flooding, and processed using the Henry2 High Performance Computing services at NC State University.

Building a Random Forest model requires the specification of several

hyperparameters. To determine the number of trees needed in the model, the model was trained using up to 1000 trees and the out of bag error was evaluated for the models with differing numbers of trees. The number of variables to possibly split at each node was determined by dividing the predictor variables by three and rounding down per Feng et al. (2015), which resulted in a value of 5. All other model hyperparameters were left constant at default values (minimum node size of 1; no limit on maximum tree depth).

2.4.2. Data splitting

Due to the large amount of non-flooded area (5,875,480 pixels) relative to flooded area (678,010 pixels), the data could not be split randomly, as such a split would have resulted in the model having fewer flooded observations in the training data, resulting in an imbalanced training set that is biased toward the majority class. To avoid an imbalanced training set, a balanced training dataset of 500,000 non-flooded pixels and 500,000 flooded pixels was created, and the leftover data were reserved as a holdout set. Upon training the model and testing it with the holdout set, model testing revealed a large rate of misclassification among non-flooded pixels; thus, the training dataset was adjusted to increase the number of non-flooded pixels represented in the training set. The resulting training set consisted of 1,000,000 non-flooded observations and 500,000 flooded observations.

2.4.3. Model performance metrics

To assess model performance, accuracy metrics were calculated based on the model's predictability on the holdout testing dataset. Overall accuracy (OA), Cohen's kappa coefficient (κ), precision (P), recall (R), specificity (S), and F1 score (F1) were calculated (Table 2). Here, OA calculates the model's overall ability to predict flood and non-flood conditions and ranges from values between 0 and 1, in which 1 is complete accuracy. κ captures the model's ability to predict considering the possibility of random agreement and values range from -1 to 1, in which values below 0 represent agreement worse than random chance, while values closer to 1 indicate that the model has better performance than a random classifier (Cohen, 1960). However, there are pitfalls to using κ (Foody, 2020), thus class-based accuracy metrics were also calculated to gauge model predictive performance. F1 is another accuracy metric that balances precision and recall for data with uneven class distributions. R is a metric ranging from 0 to 1 that highlights the model's ability to capture all flooded areas; while P quantifies the proportion of flood observations that were accurately predicted. Lastly, S was calculated to indicate how well the model could capture all the non-flood areas.

Table 2

Model performance metrics and the associated equations, range of values, and variables.

Metric	Equation	Range of values	Variables
Overall Accuracy	$OA = \frac{TP + TN}{TP + TN + FP + FN}$	0,1	TN ~ true negative count TP ~ true positive count FN ~ false negative count FP ~ false positive count
F1 Score	$F1 = \frac{2P \times R}{P + R}$	0,1	P ~ precision R ~ recall
Cohen's Kappa	$K = \frac{p_o - p_e}{1 - p_e}$	-1, 1	p_o ~ observed agreement among the two classes p_e ~ probability of random agreement.
Precision	$P = \frac{TP}{TP + FP}$	0,1	TP ~ true positive count FP ~ false positive count
Recall	$R = \frac{TP}{TP + FN}$	0,1	TP ~ true positive count FN ~ false negative count
Specificity	$S = \frac{TN}{TN + FP}$	0,1	TN ~ true negative count FP ~ false positive count

2.4.4. Variable importance

Variable importance was assessed using the permutation, or "accuracy-based," method. This method calculates importance for a variable by first reserving an out of bag sample for a tree and calculating the standard error. Then, the variable of interest is randomized while all other variables stay constant. The standard error measurement is recalculated using the new dataset containing the permuted variable. The change in error is averaged across all trees and scaled to yield the scaled permutation importance for the predictor variables. The greater the change in accuracy, the greater the importance of the variable in the model.

Given the importance of rainfall on pluvial flooding, we also analyzed which of the cumulative rainfall variables were most important in the prediction of pluvial flooding. Thus, the model performance metrics were recalculated with different rainfall variables to determine which rainfall variable was most predictive and test how the model changes with respect to antecedent rainfall. To accomplish this, the model was rerun an additional seven times with only one rainfall variable at a time and all accuracy metrics were compared between model iterations.

3. Results

3.1. Predictor variable selection

Prior to building the machine learning model, the predictor variables were screened for multicollinearity through a VIF analysis. Elevation and height above nearest drainage were highly collinear, thus elevation was omitted. Once elevation was excluded, the VIF values were less than 2 for all predictors, and all remaining predictors were used in model building.

3.2. Delineating flooded areas from Planet Labs imagery

A ROC analysis was conducted to determine the best NDWI threshold value that partitions flooded and non-flooded conditions in satellite imagery taken along the Kinston landscape. An NDWI value of 0 most effectively segregated the flood and non-flooded pixels (Fig. S2). Thus, when determining which NDWI pixels were standing water and which were not, the index values greater than 0 served to indicate inundation and values less than 0 represented dry, non-flooded areas. However, due to the sensitivity of the model to the NDWI threshold, NDWI values between -0.01 and 0.01 were labeled as NA since these pixels were right on the threshold between flooding and non-flooding. In return, these delineated NDWI rasters yielded pluvial flood maps for training the machine learning model.

3.3. Random Forest model training and testing

The model was re-trained with up to 1000 trees and out of bag error was calculated on each iteration to determine the optimal number of trees. After 750 trees, the error stabilized (Fig. S3), thus the final model used for analysis contained 750 trees.

3.4. Model performance

Model performance was assessed by calculating the P, S, R, F1, OA, and κ coefficient. These results show that the model has high S (0.97), R (0.90), F1 (0.69) and OA (0.97) values, while the P (0.56) and κ (0.68) indicate moderate agreement between predicted and observed values. The confusion matrix for the Random Forest model predictions is presented in Table S2.

3.5. Variable importance

Predictor variable importance was determined using the

permutation method (Fig. 4). Population density, distance to the nearest river, height above nearest drainage, and distance to the nearest road were the most important variables within the model. The 4-, 5-, and 6-day antecedent rainfall variables were the least important variables within the model.

Additionally, to evaluate the importance of the rainfall variables on the prediction of pluvial flooding, we compared the model performance between models with different rainfall variables. The results indicate that 3-day antecedent rainfall, 2-day antecedent rainfall, and day-of rainfall were the most important rainfall variables in predicting pluvial flooding, while 4-day, 5-day, and 6-day rainfall performed the worst (Table 3). An examination of the F1 score, which balances precision and recall, yielded that the 3-day rainfall variable was most influential in predicting pluvial flooding.

3.6. Generating flood time series

The final model was applied to create the timeline of pluvial flooding immediately after Hurricane Matthew made landfall on the Carolinas on October 8, 2016 (Fig. 5). In this case, the model is showing a snapshot of pluvial flooding at midday for each day following landfall. In the model output for Hurricane Matthew, no flooding was predicted on the day of landfall (Oct. 8), but widespread floodwaters were predicted for the following day (Oct. 9) and model predictions estimated the floodwaters mostly dissipated by Oct. 11. Interestingly, the model shows that widespread surface water flooding for Hurricane Matthew occurred on Oct. 15, seven days after landfall. Fig. S5 shows the predicted percent of flooded area for each time step of Hurricane Matthew. In addition, comparisons between the NDWI data (i.e., training/observed data) and the Random Forest model output were made to temporally gauge the model performance (Fig. 6, Fig. 7). Since these data were used to train the model, we expect higher accuracy statistics than the holdout dataset.

After generating the time series of pluvial flood dynamics, flooded croplands were inspected to discern which crops were impacted throughout the study period. The US Department of Agriculture

Table 3

Precision (P), recall (R), specificity (S), F1 score (F1), overall accuracy (OA), and Cohen's kappa (κ) for models with different rainfall variables. Each column represents the accuracy of a model with only one rainfall variable provided as a predictor.

	Day-of Rain	2 Day Rain	3 Day Rain	4 Day Rain	5 Day Rain	6 Day Rain	7 Day Rain
P	0.49	0.57	0.57	0.41	0.41	0.41	0.42
R	0.85	0.86	0.87	0.84	0.84	0.84	0.85
S	0.97	0.98	0.98	0.96	0.96	0.96	0.96
F1	0.62	0.68	0.69	0.55	0.55	0.55	0.56
OA	0.96	0.97	0.97	0.95	0.95	0.95	0.95
κ	0.6	0.67	0.67	0.53	0.53	0.53	0.54

National Agricultural Statistics Service Cropland Data Layer product (USDA NASS, 2016) was used to represent the spatial extent of different crops grown in the study region. Then, all pixels that experienced flooding from Hurricane Matthew were extracted (i.e., crop pixels that were predicted to be flooded on any day over the entire study period). The results show that corn, soybeans, and tobacco crops experienced the most flooding out of any other crops (Fig. 8).

4. Discussion

Floods are complex natural hazards that can never be fully prevented, thus it is important to be able to predict inundation and mitigate the damage. In this study, we sought to build a flood model framework that uses remotely sensed imagery and geospatial data to create pluvial flood extent maps in a flat, agricultural landscape. We demonstrated the applicability of this method in producing daily flood maps after a major storm event and evaluated key predictors in the model. Overall, the model performance metrics indicated that pluvial flooding was effectively predicted. In particular, model predictions revealed the susceptibility of croplands to pluvial flooding following extreme rainfall events, and this flood model would serve as a useful resource for flood forecasting in agriculturally dominated watersheds. Given that more

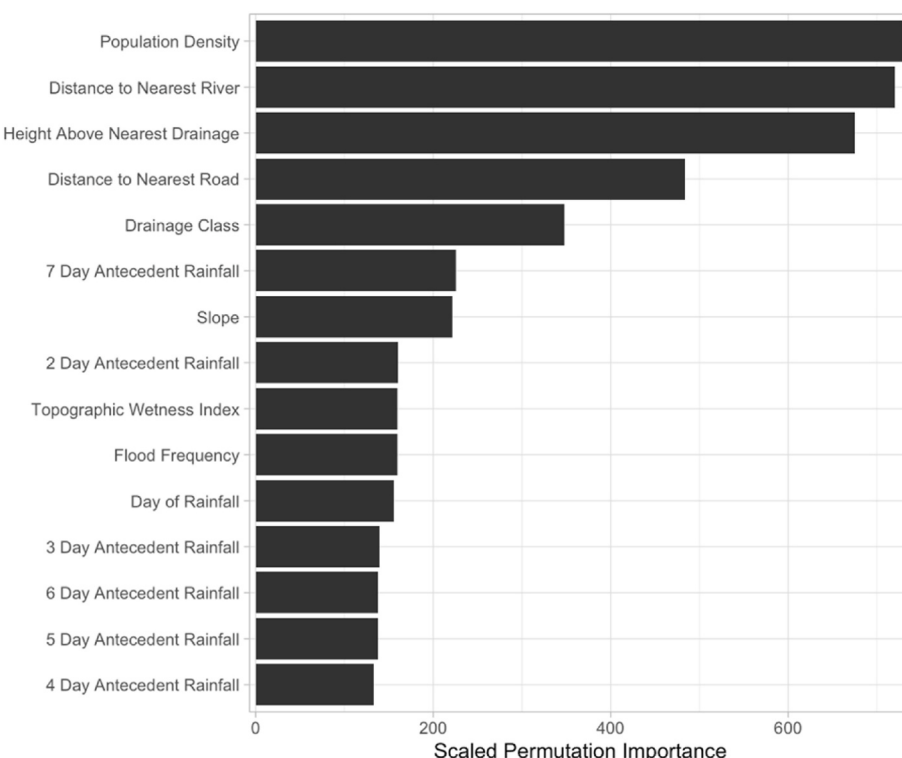


Fig. 4. Variable importance for the different predictors within the flood model.

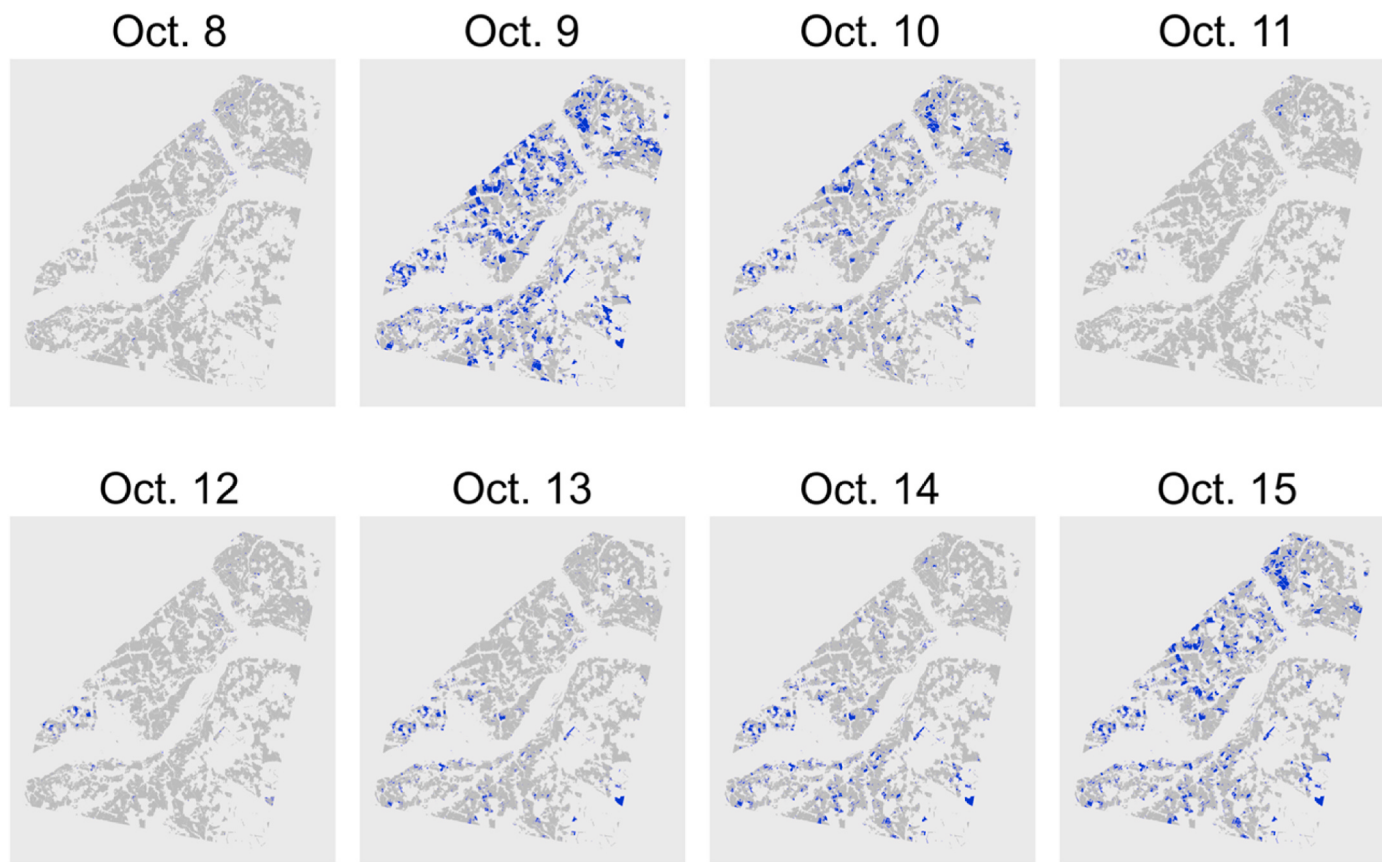


Fig. 5. Random Forest model outputs, which estimate the timeline of flooding for Hurricane Matthew from October 8–15, 2016. Blue areas represent pixels predicted to be flooded, dark gray areas represent areas predicted as non-flooded, and light gray areas are masked pixels (e.g. forested and floodplain areas).

flood studies have historically been conducted in urban areas as compared to rural, the presented modeling approach could prove effective at estimating flooding for stakeholders within other agricultural regions (e.g., [Bulti and Abebe, 2020](#); [Giustarini et al., 2013](#); [Motta et al., 2021](#); [Qi et al., 2021](#)).

Overall, the flood model results show that the performance was good (OA of 0.97, κ of 0.68), with the errors largely attributed to false positives. The S of 0.97 and R of 0.90 indicate that the model can correctly predict 97% of the non-flooded pixels and 90% of the flooded pixels. However, the P of this model (0.56) is not as high as the other examined performance metrics, which indicates that there is a large presence of false positives produced from the model. False positive predictions also explain the difference between the F1 score (0.69) and OA (0.97). We believe the large presence of false positives could be attributed to the quality of the data, as some landscape features appear to have similar reflectance values as water features. However, the occurrence of false positives is not necessarily a poor result in the context of disaster response, since the detection of false positives is generally considered better than false negatives. False positives are preferable to false negatives since false positives might lead to individuals in an area preparing for a flood that may not occur, which would be better than misleading individuals into thinking their area will not flood, only to have them suffer from devastating inundation.

Closer inspection of differences between NDWI (i.e., observed data) and predicted flooding provided insights as to where model performance suffered. We investigated the discrepancies between NDWI and the pluvial flood predictions by zooming into a portion of the landscape ([Fig. 7](#)), which revealed that the Random Forest model often misclassified boundaries of flooded areas. However, it is important to note that the training data produced by thresholding NDWI could inherently have error, as it was determined through an ROC analysis. Thus, since

NDWI values cannot be taken as absolute truth, we are limited in our ability to fully understand the final error of our model as the error from the ROC analysis would have propagated into the final pluvial model's outputs. Still, visual inspection of the outputs demonstrates that the source of the false positives is largely from the pixels immediately surrounding flooded areas, which indicates the false positives are not spurious.

An examination of predictor variable performance shows that geophysical predictors were the most important in the flood model, specifically distance to the nearest stream, distance to the nearest road, and height above nearest drainage. Thus, the importance of these variables highlights the value of physically-based geospatial products in flood prediction. The distance to nearest road variable serves as an interesting predictor variable that we anticipate was deemed important due to how roads are designed to quickly route water off roads, which can lead to water pooling and flooding ([Kalantari, 2014](#)). It is important to note that we consider pluvial flooding to be the flood extent outside the boundaries of the channel and floodplain. Therefore, it is possible that fluvial processes have an influence on the flooding in this analysis, which is an explanation for the importance of height above nearest drainage and distance to nearest stream within the model. Furthermore, it is difficult to completely separate the pluvial and fluvial processes from one another in this analysis because (1) lands near streams are likely experiencing flooding from heavy rainfall leading to soil saturation and overflow of the channel and floodplain, processes which are challenging to separate in flat terrain, and (2) when the channel is full it also impacts the upstream ditches that cannot drain due to backwater conditions, which leads to or exacerbates flooding. Overall, we assume that there is some influence of fluvial processes on the pluvial flooding modeled in this study, but we could not quantify the degree of influence.

Interestingly, population density served as the most important

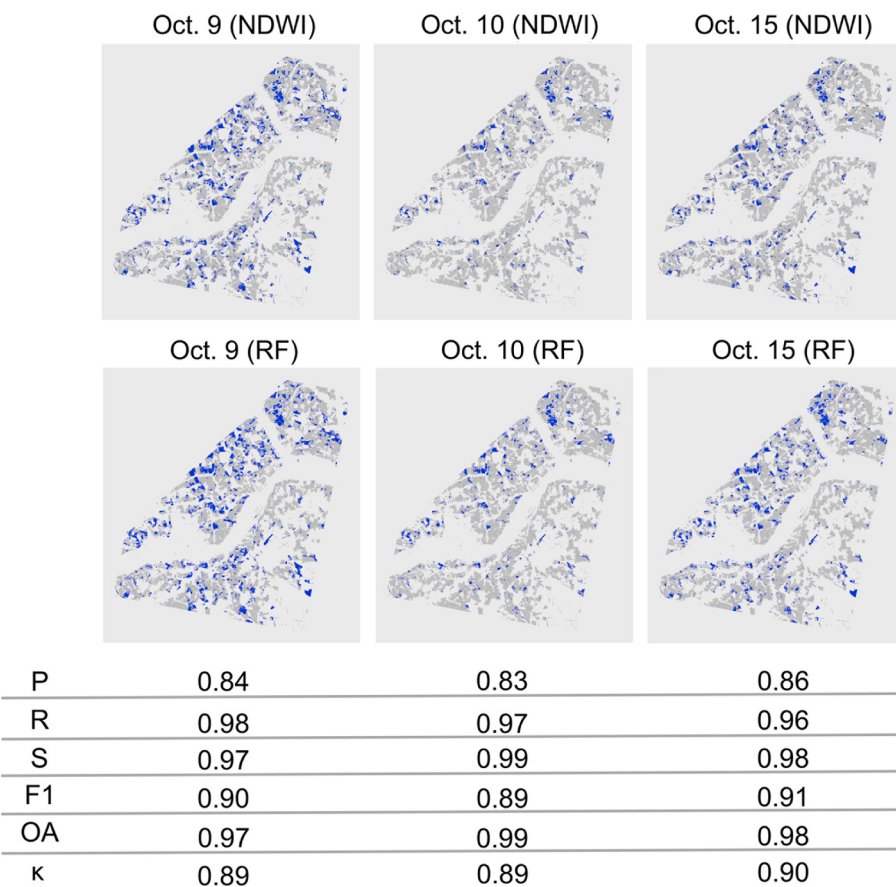


Fig. 6. Comparison of NDWI data and Random Forest (RF) model predictions for Oct. 9, 10, and 15. Temporal-based accuracy statistics, shown below the flood maps, were calculated for each date.

variable within the model, although numerous model iterations revealed that population density was comparable to height above nearest drainage and distance to nearest stream in predictive performance. Rural populations are highly exposed to flooding, with one study finding that hotspots with high flood exposure were primarily rural (based on population density), and these areas were typically characterized by high social vulnerability as well (Tate et al., 2021). In our study area, the highest population densities primarily occurred in pixels adjacent to masked developed areas (Fig. 1, Fig. S6), which were also areas with relatively denser road networks. Accordingly, these are likely areas with higher impervious surfaces, less potential for rain infiltration, and greater risk of ponding, which could help explain the relative importance of population density as a predictor variable despite the low overall population densities in our rural study area.

While population density and geophysical predictors were most important in the model, 4-day rainfall, 5-day rainfall, and 6-day rainfall were the least important variables. An evaluation of model performance considering only one cumulative rainfall at a time yielded that the 3-day rainfall, 2-day rainfall, and day-of rainfall were the most important in predicting pluvial flooding, respectively. The importance of 3-, 2-, and day-of rainfall relative to 4-, 5-, and 6-day rainfall totals in the model indicates there was minimal lag time between rainfall and pluvial flooding. Whereas a longer separation between fluvial flooding and rainfall may be expected due to variation in a watershed's time of concentration, we would expect pluvial flooding to respond to near-term rainfall given it is largely driven by ponding rather than surface water flow. Thus, the importance of near-term rainfall variables aligns with our mechanistic understanding of pluvial flooding drivers. However, it is worth noting that the rainfall data was resampled from 1-km to 10-m resolution, and variable importance results may have differed had

finer resolution rainfall data been available and used in model development.

Topographic wetness index and flood frequency were relatively moderate predictors of pluvial flooding within the model. Topographic wetness may not have been as important in the model due to the correlation between height above nearest drainage and topographic wetness, as both variables are derived from elevation data. Most likely, the height above nearest drainage variable is capturing the influence of elevation on flooding, thus making the topographic wetness index less important, comparatively. Similarly, flood frequency was a moderately important variable within each model training iteration. However, the masking of wooded wetlands and the floodplain, which surrounded rivers in the area, likely explains why the flood frequency product was not more important of a predictor of pluvial flooding. The “high risk” flood frequency designations primarily occur in stream or river floodplains; thus, masking woody wetlands and floodplain areas likely would have largely removed most of the “high risk” areas from consideration during model application. Future work should experiment with combinations of physical predictor variables that avoid overfitting and produce high accuracy.

Lastly, the flood timeline from Hurricane Matthew was created by applying the final Random Forest model. Maps of model predictions show that pluvial flooding persisted in Kinston for about two days following Hurricane Matthew. The model outputs demonstrated that no flooding was predicted on the day of landfall, which may be due to the rainfall from the storms having not yet saturated soils across on the landscape (the peak rainfall occurred after midday on Oct. 8). However, beginning the day following landfall, the model predicted that flooding began. Curiously, the model predicted a resurgence of flooding on Oct. 15: model outputs show an initial flood peak occurring one day after

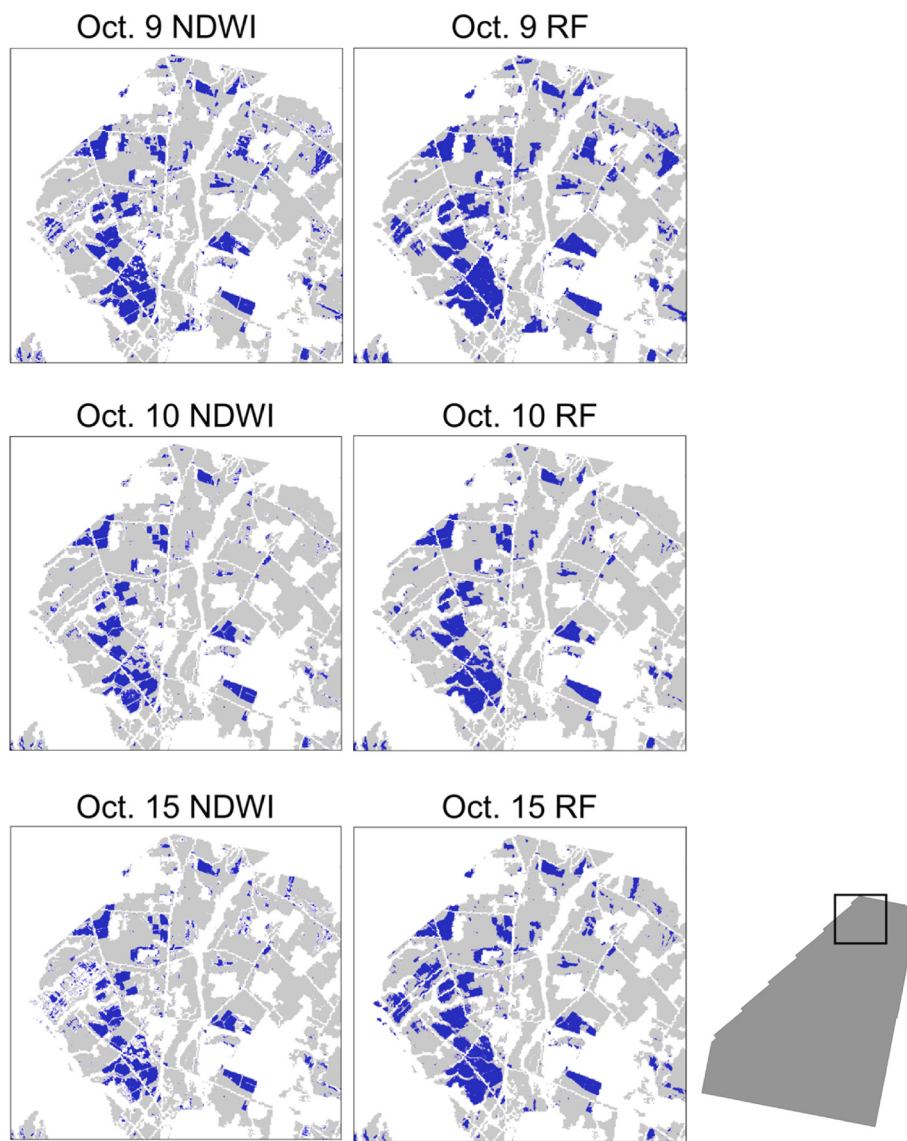


Fig. 7. A zoomed in portion of the study area comparing the NDWI flood maps to the Random Forest (RF) model outputs.

landfall (Oct. 9), the floodwaters subsequently retreating, and then a second peak occurring on Oct. 15. Although model testing indicated the model had high performance, we are unable to confirm whether this resurgence occurred in reality. However, we believe that this resurgence is not actually occurring, as the model is likely not capturing the full extent of flooding on days without satellite observations. This may be due to a lack of temporal data or the model's inability to capture temporal dependencies of flood dynamics (e.g., if it is flooded on day 1 and day 3, then it is likely to be flooded on day 2).

Overall, the flood timeline associated with Hurricane Matthew revealed that pluvial flooding was not widespread across the landscape, leading us to believe that drainage within agricultural soils was effective in reducing the extent of waterlogging. It is worth noting that artificial drainage methods are used in the study area. Although information on the extent of drainage practices would be ideal, we do not have a data product that captures the geospatial locations of drainage systems. Thus, given how extensive poorly drained soils are in the area (Fig. S7), we suspect the use of artificial drainage (e.g., ditching and tiles) could be contributing to the lack of flooding in some agricultural landscapes.

Further evaluation of the croplands that were flooded across the landscape yielded that corn and soybean fields were the crops that were primarily affected by Hurricane Matthew (Fig. 8). This is an important

consideration for local farmers, as flood conditions deplete soil oxygen and affect plant growth. Specifically, corn, tobacco, and soybeans are crops sensitive to waterlogging, particularly in the early stages of growth (Kaur et al., 2019; Nurhidayati et al., 2021; Purnobasuki et al., 2018; Rhine et al., 2010; Scott et al., 1989; Walne and Reddy, 2021). Model outputs could be used to identify areas with relatively low risk of pluvial flooding, which could then be areas better suited for planting crops that are sensitive to water stress. Interestingly, cotton is highly sensitive to excess rain in the seedling and boll opening stages (Hake et al., 1992), and the lack of flooding in cotton fields suggests that growers may already have adapted their planting patterns based on prior pluvial flooding experiences, indicating that crop type may be an effective pluvial flooding predictor.

The framework and methods presented in this study are transferable; however, model application cannot be transferred to new regions without any adaptation to the model. This is due to the machine learning model deriving specific relationships from the data collected in rural North Carolina, which may not be characteristic of other agricultural landscapes. Additionally, although other models exist for fluvial, coastal, and urban flooding, the mechanisms that generate flooding in these systems are different compared to rural pluvial flooding. Thus, the approach outlined in this work presents a simplified framework for

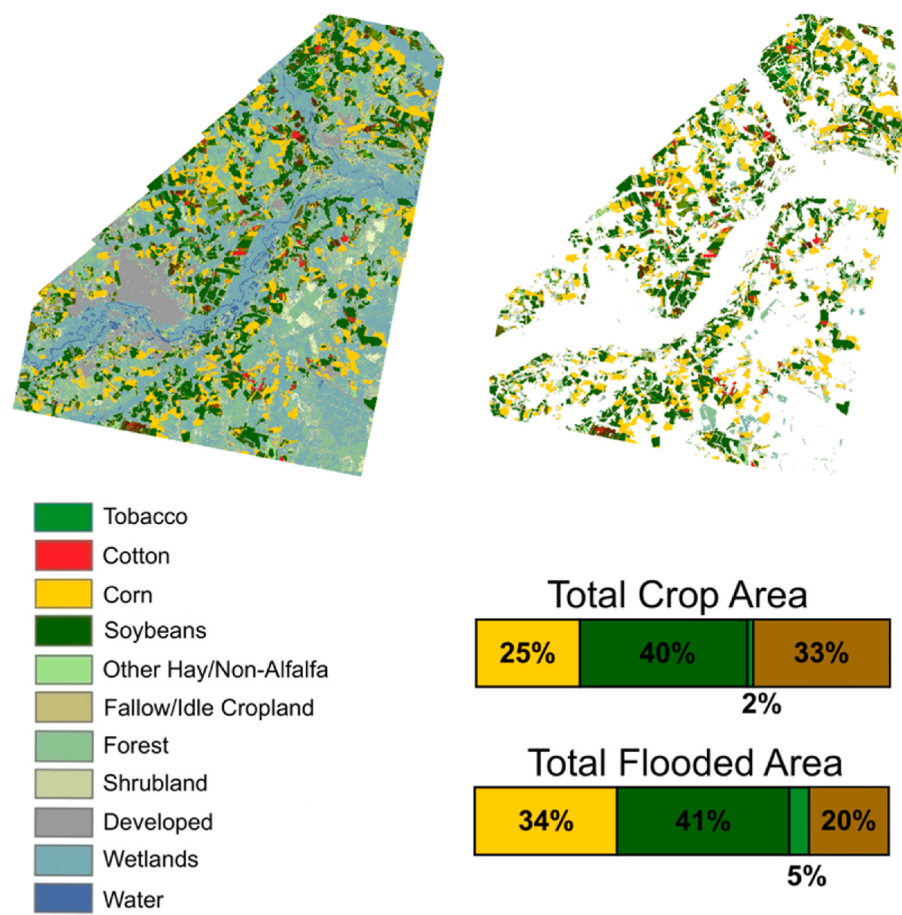


Fig. 8. US Department of Agriculture National Agricultural Statistics Service Cropland Data Layer product for the Kinston area during Hurricane Matthew. The left map depicts the cropland data layer product, while the right map depicts the same product after the masking process. The legend on the left depicts the color associated with the dominant crop classifications for the area. The bar chart shows the percent of total and flooded area for corn (yellow), soybeans (dark green), tobacco (medium green), and all other crop classifications (brown), respectively.

predicting pluvial flood extent and highlighting predictors of flooding in agricultural landscapes using high-resolution remotely sensed imagery and open-access geospatial data layers for an area of interest.

5. Conclusions

Flat, low-lying landscapes are notorious for flooding as well as being difficult areas in which to predict inundation. Current flood studies focus on the dynamics of flooding in urban, riverine, and coastal systems; however, agricultural landscapes are prone to flooding which can cause disruptions to food security and farmers' livelihoods. To address this problem, this study developed a Random Forest flood model for the prediction of daily flood extent in agricultural lands and evaluated characteristics of areas prone to pluvial flooding. The present work contributes to current flood modeling research by developing a machine learning model that predicts daily dynamics of pluvial flooding in a low-terrain and agricultural landscape, allowing for estimation and illustration of the surge and retreat of floodwaters. The structure of the model is such that, as more satellite imagery and flood data are generated, more training data could be fed into the model for better predictability, allowing the model to improve over time. The trained model could also be used in a forecasting context to predict flooding under future precipitation, land cover, and geophysical conditions.

The flood model performance indicated high accuracy, with errors attributed largely to false positives. A comparison between the NDWI flood maps and the model outputs demonstrated that most of the false positives corresponded to pixels adjacent to areas identified as flooded using NDWI. The performance of the flood model may be improved with ground truth data that corroborates the flood conditions of the pixels. Another potential concern is the model's lack of flood prediction on dates without satellite imagery. The NDWI used to train the model

showed that the flood extent was slightly less on Oct. 10, compared to Oct. 9 and 15. The Random Forest model predicted little flooding between Oct. 11–14; however, we are unsure if this retreat and then resurgence of flooding on Oct. 15 is an actual occurrence. It is possible the model predicted a decrease in flooding leading up to the 15th because of the rain patterns observed in the study area (Fig. 2). It is also possible that there are fluvial processes that are impacting the pluvial flood extent on Oct. 15, when riverine flow rates were high. By supplementing the model with more flood data from future hurricane events, we may be able to dissect this discrepancy; however, at the moment, this finding remains an uncertainty.

In regard to predictor performance, population density, distance to the nearest stream, distance to the nearest road, and height above nearest drainage, were the most important in flood extent prediction. Meanwhile, the 4-day, 5-day, and 6-day cumulative rainfall were the least important variables in the model.

A key limitation of the model is the mere lack of available flood data, as even the characterization of flooding is a contemporary challenge. Therefore, it is unlikely that we were able to capture all pluvial flooding across the landscape. Despite the pitfalls, the high performance of the model indicates that this tool has the potential to be a valuable resource for flood management in agriculturally dominated watersheds. In addition, this Random Forest flood model may be used to inform farmers which areas and crops are suspected to flood, as well as the duration of flooding, when used with forecasted rainfall information.

In the future, process-based and machine learning methods may be combined to predict flooding in agricultural landscapes without the reliance of satellite imagery. The coupling of process-based and data-driving models has the potential of representing system dynamics using the complementary strengths of each modeling method. Such process-guided machine learning models would allow for a

generalizable pluvial model that is able to accurately account for unseen scenarios using the laws of mass and energy transfer.

Declaration of competing interest

The authors declare that they have no known competing financial interests or personal relationships that could have appeared to influence the work reported in this paper.

Data availability

The Planet Labs data are proprietary, but all other analyzed data are free and publicly available.

Acknowledgments

The authors report no conflicts of interests and thank Dr. Brian Reich for sharing feedback on the statistical approach used in the study.

This work was supported by the National Science Foundation RAPID grant 1901588; NC Space Grant Graduate Research Fellowship under NASA Grant NNX15AH81H; U.S. Department of Agriculture Food and Agriculture Cyberinformatics and Tools (FACT) project (2019-67021-29936); U.S. Department of Agriculture National Institute of Food and Agriculture (NIFA) Hatch project 1016068.

Appendix A. Supplementary data

Supplementary data to this article can be found online at <https://doi.org/10.1016/j.envsoft.2023.105758>.

References

- Abebe, Y., Kabir, G., Tesfamariam, S., 2018. Assessing urban areas vulnerability to pluvial flooding using GIS applications and Bayesian Belief Network model. *J. Clean. Prod.* 174, 1629–1641. <https://doi.org/10.1016/j.jclepro.2017.11.066>.
- Bernet, D.B., Zischg, A.P., Prasuhn, V., Weingartner, R., 2018. Modeling the extent of surface water floods in rural areas: lessons learned from the application of various uncalibrated models. *Environ. Model. Software* 109, 134–151. <https://doi.org/10.1016/j.envsoft.2018.08.005>.
- Botzen, W.J.W., Aerts, J.C.J.H., van den Bergh, J.C.J.M., 2012. Individual preferences for reducing flood risk to near zero through elevation. *Mitig. Adapt. Strategies Glob. Change* 2, 229–244. <https://doi.org/10.1007/s11027-012-9359-5>.
- Breiman, L., 2001. Random forests. *Mach. Learn.* 45, 5–32. <https://doi.org/10.1023/A:1010933404324>.
- Bulti, D.T., Abebe, B.G., 2020. A review of flood modeling methods for urban pluvial flood application. *Modeling Earth Systems and Environment* 6 (3), 1293–1302. <https://doi.org/10.1007/s40808-020-00080-z>.
- Chen, W., Li, Y., Xue, W., Shahabi, H., Li, S., Hong, H., et al., 2020. Modeling flood susceptibility using data-driven approaches of naïve Bayes tree, alternating decision tree, and random forest methods. *Sci. Total Environ.* 701, 134979 <https://doi.org/10.1016/j.scitotenv.2019.134979>.
- Choubin, B., Moradi, E., Golshan, M., Adamowski, J., Sajedi-Hosseini, F., Mosavi, A., 2019. An ensemble prediction of flood susceptibility using multivariate discriminant analysis, classification and regression trees, and support vector machines. *Sci. Total Environ.* 651, 2087–2096. <https://doi.org/10.1016/j.scitotenv.2018.10.064>.
- Cohen, J., 1960. A coefficient of agreement for nominal scale. *Educ. Psychol. Meas.* 20, 37–46. <https://doi.org/10.1177/001316446002000104>.
- Costache, R., Popa, M.C., Tien Bui, D., Diaconu, D.C., Ciubotaru, N., Minea, G., Pham, Q. B., 2020. Spatial predicting of flood potential areas using novel hybridizations of fuzzy decision-making, bivariate statistics, and machine learning. *J. Hydrol.* 585, 124808 <https://doi.org/10.1016/j.jhydrol.2020.124808>.
- Dewitz, J., 2019. National Land Cover Database (NLCD) 2016 Products. U.S. Geological Survey data release. <https://doi.org/10.5066/P96HHBIE>.
- Dietterich, T.G., 2000. Ensemble methods in machine learning. In: Int. Workshop on Multiple Classifier Systems, pp. 1–15. https://doi.org/10.1007/3-540-45014-9_1.
- FEMA. National Flood Hazard Layer, 2019. Version 1.1.1.0. <https://www.fema.gov/flood-maps/national-flood-hazard-layer>.
- Feng, Q., Gong, J., Liu, J., Li, Y., 2015. Flood mapping based on multiple endmember spectral mixture analysis and random forest classifier—the case of yuyao, China. *Rem. Sens.* 7 (9), 12539–12562. <https://doi.org/10.3390/rs70912539>.
- First Street Foundation, 2020. The First National Flood Risk Assessment: Defining America's Growing Risk. https://assets.firststreet.org/uploads/2020/06/first_street.foundation._first.national.flood.risk.assessment.pdf.
- Foody, G.M., 2020. Explaining the unsuitability of the kappa coefficient in the assessment and comparison of the accuracy of thematic maps obtained by image classification. *Remote Sens. Environ.* 239, 111630 <https://doi.org/10.1016/j.rse.2019.111630>.
- Giustarini, L., Matgen, P., Hostache, R., Guy, S., Bates, P.D., Mason, C., 2013. A change detection approach to flood mapping in urban areas using TerraSAR-X. *IEEE Trans. Geosci. Rem. Sens.* <https://doi.org/10.1109/TGRS.2012.2210901>.
- Guerreiro, S.B., Glenis, V., Dawson, R.J., Kilsby, C., 2017. Pluvial flooding in European cities—a continental approach to urban flood modelling. *Water* 9 (4), 296. <https://doi.org/10.3390/w9040296>.
- Hake, K., Krieg, D., Landivar, J., Oosterhuis, D., 1992. Plant water relations. *Cotton Physiology Today* 3 (7). <http://www.cotton.org/tech/physiology/cpt/plantphysiology/upload/CPT-July92-REPOP.pdf>.
- Hou, J., Zhou, N., Chen, G., Huang, M., Bai, G., 2021. Rapid forecasting of urban flood inundation using multiple machine learning models. *Nat. Hazards* 108, 2335–2356. <https://doi.org/10.1007/s11069-021-04782-x>.
- Jain, S.K., Mani, P., Jain, S.K., Prakash, P., Singh, V.P., Tullos, D., et al., 2018. A Brief review of flood forecasting techniques and their applications. *Int. J. River Basin Manag.* 16 (3), 329–344. <https://doi.org/10.1080/15715124.2017.1411920>.
- Jongman, B., Ward, P.J., Aerts, J.C.J.H., 2012. Global exposure to river and coastal flooding: long term trends and changes. *Global Environ. Change* 22 (4), 823–835. <https://doi.org/10.1016/j.gloenvcha.2012.07.004>.
- Kabir, S., Patidar, S., Pender, G., 2021. A machine learning approach for forecasting and visualising flood inundation information. *Proc. Inst. Civ. Eng.: Water Management* 174 (1), 27–41. <https://doi.org/10.1680/jwama.20.00002>.
- Kalantari, Z., 2014. A method for mapping flood hazard along roads. *J. Environ. Manag.* 133 (15), 69–77. <https://doi.org/10.1016/j.jenvman.2013.11.032>.
- Kan, G., Liang, K., Yu, H., Sun, B., Ding, L., Li, J., et al., 2020. Hybrid machine learning hydrological model for flood forecast purpose. *Open Geosci.* 12 (1), 813–820. <https://doi.org/10.1515/geo-2020-0166>.
- Kauffeldt, A., Wetterhall, F., Pappenberger, F., Salomon, P., Thielen, J., 2016. Technical review of large-scale hydrological models for implementation in operational flood forecasting schemes on continental level. *Environ. Model. Software* 75, 68–76. <https://doi.org/10.1016/j.envsoft.2015.09.009>.
- Kaur, G., Zurweller, B., Motavalli, P.P., Nelson, K.A., 2019. Screening corn hybrids for soil waterlogging tolerance at an early growth stage. *Agriculture* 9 (2), 33. <https://doi.org/10.3390/agriculture9020033>.
- Khosravi, K., Pham, B.T., Chapi, K., Shirzadi, A., Shahabi, H., Revhaug, I., et al., 2018. A comparative assessment of decision trees algorithms for flash flood susceptibility modeling at Haraz watershed, northern Iran. *Sci. Total Environ.* 627, 744–755. <https://doi.org/10.1016/j.scitotenv.2018.01.266>.
- Li, Z., Liu, H., Luo, C., Fu, G., 2021. Assessing surface water flood risks in urban areas using machine learning. *Water* 13 (24), 3520. <https://doi.org/10.3390/w13243520>.
- Marquardt, D.W., 1970. Generalized inverses, ridge regression, biased linear estimation, and nonlinear regression. *Technometrics* 12, 591–613.
- McFeeters, 1996. The use of the normalized difference water index (NDWI) in the delineation of open water features. *Int. J. Rem. Sens.* 17 (7), 1425–1432. <https://doi.org/10.1080/0143169608948714>.
- Mosavi, A., Ozturk, P., Chau, K.W., 2018. Flood prediction using machine learning models: literature review. *Water (Switzerland)* 10 (11), 1–40. <https://doi.org/10.3390/w10111536>.
- Motta, M., de Castro Neto, M., Sarmento, P., 2021. A mixed approach for urban flood prediction using Machine Learning and GIS. *Int. J. Disaster Risk Reduc.* 56, 102154 <https://doi.org/10.1016/j.ijdrr.2021.102154>.
- Muthusamy, M., Casado, M.R., Salmorai, G., Irvine, T., Leinster, P., 2019. A remote sensing based integrated approach to quantify the impact of fluvial and pluvial flooding in an urban catchment. *Rem. Sens.* 11 (5), 577. <https://doi.org/10.3390/rs11050577>.
- NC Department of Transportation (NCDOT), 2002. Roadway Design Manual General Design Information, Design Criteria and Plan Preparation Guides. <https://connect.ncdot.gov/projects/Roadway/pages/roadway-design-manual.aspx>.
- NC Department of Transportation (NCDOT), 2018. Roadway Standard Drawings. <https://connect.ncdot.gov/resources/Specifications/Pages/2018-Roadway-Standrd-Drawings.aspx>.
- NOAA National Centers for Environmental Information (NCEI), 2021. U.S. Billion-Dollar Weather and Climate Disasters. <https://doi.org/10.25921/stkw-7w73>. <https://www.ncdc.noaa.gov/billions/>.
- NOAA National Severe Storms Laboratory (NSSL). (n.d.) SEVERE WEATHER 101—Floods <https://www.nssl.noaa.gov/education/srvwx101/floods/>.
- Nurhidayati, T., Safitri, W.Y., Purnobasuki, H., Hariyanto, S., 2021. Response of tobacco (*Nicotiana tabacum L.*) under waterlogging stress based on agronomic characters. *AIP Conf. Proc.* 2349, 020019 <https://doi.org/10.1063/5.0051852>.
- Palla, A., Colli, M., Candela, A., Aronica, G.t., Lanza, L.g., 2018. Pluvial flooding in urban areas: the role of surface drainage efficiency. *Journal of Flood Risk Management* 11 (S2), S663–S676. <https://doi.org/10.1111/jfr3.12246>.
- Purnobasuki, H., Nurhidayati, T., Hariyanto, S., Jadid, N., 2018. Data of root anatomical responses to periodic waterlogging stress of tobacco (*Nicotiana tabacum*) varieties. *Data Brief* 20, 2012–2016. <https://doi.org/10.1016/j.dib.2018.09.046>.
- Qi, W., Ma, C., Xu, H., Chen, Z., Zhao, K., Han, H., 2021. A review on applications of urban flood models in flood mitigation strategies. *Nat. Hazards* 108, 31–62. <https://doi.org/10.1007/s11069-021-04715-8>.
- R Core Team, 2020. R: A Language and Environment for Statistical Computing. R Foundation for Statistical Computing, Vienna, Austria. <https://www.R-project.org/>.
- Rennó, C.D., Nobre, A.D., Cuartas, L.A., Soares, J.V., Hodnett, M.G., Tomasella, J., Waterloo, M.J., 2008. HAND, a new terrain descriptor using SRTM-DEM: mapping terra-firme rainforest environments in Amazonia. *Remote Sens. Environ.* 112 (9), 3469–3481. <https://doi.org/10.1016/j.rse.2008.03.018>.

- Rhine, M.D., Stevens, G., Shannon, G., Wrather, A., Sleper, D., 2010. Yield and nutritional responses to waterlogging of soybean cultivars. *Irrigat. Sci.* 28, 135–142. <https://doi.org/10.1007/s00271-009-0168-x>.
- Rose, A.N., McKee, J.J., Sims, K.M., Bright, E.A., Reith, A.E., Urban, M.L., 2020. *LandScan 2019*. Oak Ridge National Laboratory.
- Scott, H.D., DeAngulo, J., Daniels, M.B., Wood, L.S., 1989. Flood duration effects on soybean growth and yield. *Agron. J.* 81 (4), 631–636. <https://doi.org/10.2134/agronj1989.00021962008100040016x>.
- Soil Survey Staff, 2019. Gridded soil Survey geographic (gSSURGO) Database for North Carolina. United States department of agriculture, natural resources conservation service. <http://datagateway.ncrcs.usda.gov/>.
- Stewart, S.R., 2017. National hurricane center tropical cyclone report: hurricane Matthew (AL142016). https://www.nhc.noaa.gov/data/tcr/AL142016_Matthew.pdf.
- Tabbassum, R., Dar, A.Q., 2021. Modelling hybrid and backpropagation adaptive neuro-fuzzy inference systems for flood forecasting. *Nat. Hazards*, 0123456789. <https://doi.org/10.1007/s11069-021-04694-w>.
- Tanir, T., de Lima, A.de S., de A. Coelho, G., Uzun, S., Cassalho, F., Ferreira, C.M., 2021. Assessing the spatiotemporal socioeconomic flood vulnerability of agricultural communities in the Potomac River Watershed. *Nat. Hazards* 108 (1), 225–251. <https://doi.org/10.1007/s11069-021-04677-x>.
- Tate, E., Rahman, M.A., Emrich, C.T., Sampson, C.C., et al., 2021. Flood exposure and social vulnerability in the United States. *Nat. Hazards* 106, 435–457. <https://doi.org/10.1007/s11069-020-04470-2>.
- Tebrany, M.S., Jones, S., Shabani, F., 2019. Identifying the essential flood conditioning factors for flood prone area mapping using machine learning techniques. *Catena* 175 (April 2018), 174–192. <https://doi.org/10.1016/j.catena.2018.12.011>.
- Tebrany, M.S., Pradhan, B., Mansor, S., Ahmad, N., 2015. Flood susceptibility assessment using GIS-based support vector machine model with different kernel types. *Catena* 125, 91–101. <https://doi.org/10.1016/j.catena.2014.10.017>.
- Tellman, B., Sullivan, J.A., Kuhn, C., Kettner, A.J., Doyle, C.S., Brakenridge, G.R., et al., 2021. Satellite imaging reveals increased proportion of population exposed to floods. *Nature* 596, 80–86. <https://doi.org/10.1038/s41586-021-03695-w>.
- Teng, J., Jakeman, A.J., Vaze, J., Croke, B.F.W., Dutta, D., Kim, S., 2017. Flood inundation modelling: a review of methods, recent advances and uncertainty analysis. *Environ. Model. Software* 90, 201–216. <https://doi.org/10.1016/j.envsoft.2017.01.006>.
- Thornton, M.M., Shrestha, R., Wei, Y., Thornton, P.E., Kao, S., Wilson, B.E., 2020. Daymet: Daily Surface Weather Data on a 1-km Grid for North America. Version 4. ORNL DAAC, Oak Ridge, Tennessee, USA. <https://doi.org/10.3334/ORNLDAC/1840>.
- Towfiqul Islam, A.R.M., Talukdar, S., Mahato, S., Kundu, S., Eibek, K.U., Pham, Q.B., et al., 2021. Flood susceptibility modelling using advanced ensemble machine learning models. *Geosci. Front.* 12 (3) <https://doi.org/10.1016/j.gsf.2020.09.006>.
- U.S. Census Bureau, 2015. TIGER/Line Streets 2015 Dataset. <https://www.census.gov/geographies/mapping-files/time-series/geo/tiger-line-file.html>.
- USDA National Agricultural Statistics Service (NASS) Cropland Data Layer, 2016. Published crop-specific data layer [Online]. USDA-NASS, Washington, DC. <https://nassgeodata.gmu.edu/CropScape/>.
- U.S. Geological Survey, 2019a. National elevation dataset 10-meter resolution digital elevation model (published 20200606). <https://www.usgs.gov/core-science-systems/ngp/3dep/data-tools>. (Accessed 23 October 2019).
- U.S. Geological Survey, 2019b. National Hydrography Dataset Best Resolution (NHD) for Hydrologic Unit (HU) 4 - 2001 (published 20191002). <https://www.usgs.gov/core-science-systems/ngp/national-hydrography/access-national-hydrography-products>.
- van Dijk, E., van der Meulen, J., Kluck, J., Straatman, J.H.M., 2013. Comparing modelling techniques for analysing urban pluvial flooding. *Water Sci. Technol.* 69 (2), 305–311. <https://doi.org/10.2166/wst.2013.699>.
- Walne, C.H., Reddy, K.R., 2021. Developing functional relationships between soil waterlogging and corn shoot and root growth and development. *Plants* 10 (10), 2095. <https://doi.org/10.3390/plants10102095>.
- World Health Organization (WHO). (n.d.) Floods. <https://www.who.int/health-topics/floods>.
- Wright, M.N., Ziegler, A., 2017. ranger: a fast implementation of random forests for high dimensional data in C++ and R. *J. Stat. Software* 77, 1–17. <https://doi.org/10.18637/jss.v077.i01>.
- Yeditha, P.K., Kasi, V., Rathinasamy, M., Agarwal, A., 2020. Forecasting of extreme flood events using different satellite precipitation products and wavelet-based machine learning methods. *Chaos* 30 (6), 1–12. <https://doi.org/10.1063/5.0008195>.
- Zakaria, M.N.A., Abdul Malek, M., Zolkepli, M., Najah Ahmed, A., 2021. Application of artificial intelligence algorithms for hourly river level forecast: a case study of Muda River, Malaysia. *Alex. Eng. J.* 60 (4), 4015–4028. <https://doi.org/10.1016/j.cej.2021.02.046>.